

# The Effects of Specimen Geometry on the Plastic Deformation of AA 2219-T8 Aluminum Alloy Under Dynamic Impact Loading

G.M. Owolabi, D.T. Bolling, A.G. Odeshi, H.A. Whitworth, N. Yilmaz, and A. Zeytinci

(Submitted May 17, 2017; in revised form July 28, 2017; published online November 13, 2017)

The effects of specimen geometry on shear strain localization in AA 2219-T8 aluminum alloy under dynamic impact loading were investigated. The alloy was machined into cylindrical, cuboidal and conical (frustum) test specimens. Both deformed and transformed adiabatic shear bands developed in the alloy during the impact loading. The critical strain rate for formation of the deformed band was determined to be  $2500 \text{ s}^{-1}$  irrespective of the specimen geometry. The critical strain rate required for formation of transformed band is higher than  $3000 \text{ s}^{-1}$  depending on the specimen geometry. The critical strain rate for formation of transformed bands is lowest ( $3000 \text{ s}^{-1}$ ) in the  $\text{Ø}5 \text{ mm} \times 5 \text{ mm}$  cylindrical specimens and highest ( $> 6000 \text{ s}^{-1}$ ) in the conical specimens. The cylindrical specimens showed the greatest tendency to form transformed bands, whereas the conical specimen showed the least tendency. The shape of the shear bands on the impacted plane was also observed to be dependent on the specimen geometry. Whereas the shear bands on the compression plane of the conical specimens formed elongated cycles, two elliptical shaped shear bands facing each other were observed on the cylindrical specimens. Two parallel shear bands were observed on the compression planes of the cuboidal specimens. The dynamic stress–strain curves vary slightly with the specimen geometry. The cuboidal specimens exhibit higher tendency for strain hardening and higher maximum flow stress than the other specimens. The microstructure evolution leading to the formation of transformed bands is also discussed in this paper.

**Keywords** AA 2219 aluminum alloy, adiabatic shear bands, dynamic impact loading, failure, plastic deformation

## 1. Introduction

AA 2219 aluminum alloy is an aluminum-copper alloy that is widely used in the aerospace and defense industry due to their high specific strength and excellent weldability. It is useful for cryogenic applications while it can also retain its good mechanical properties up to  $250 \text{ °C}$  (Ref 1, 2). As a result of its high tensile strength and good ductility at cryogenic temperatures, excellent weldability and good resistance to stress corrosion cracking, AA 2219 aluminum alloy is an attractive material for construction of propellant tanks (Ref 3) and storage tanks for liquid nitrogen and oxygen (Ref 2). Its high temperature capability also makes it a candidate material for the fabrication of large molds for polymer casting (Ref 4). Narayana et al. (Ref 1) investigated the tensile and fracture behavior of rolled AA 2219-T87 aluminum alloy plate along transverse and longitudinal directions and reported a uniform distribution of densely packed fine precipitates along each of

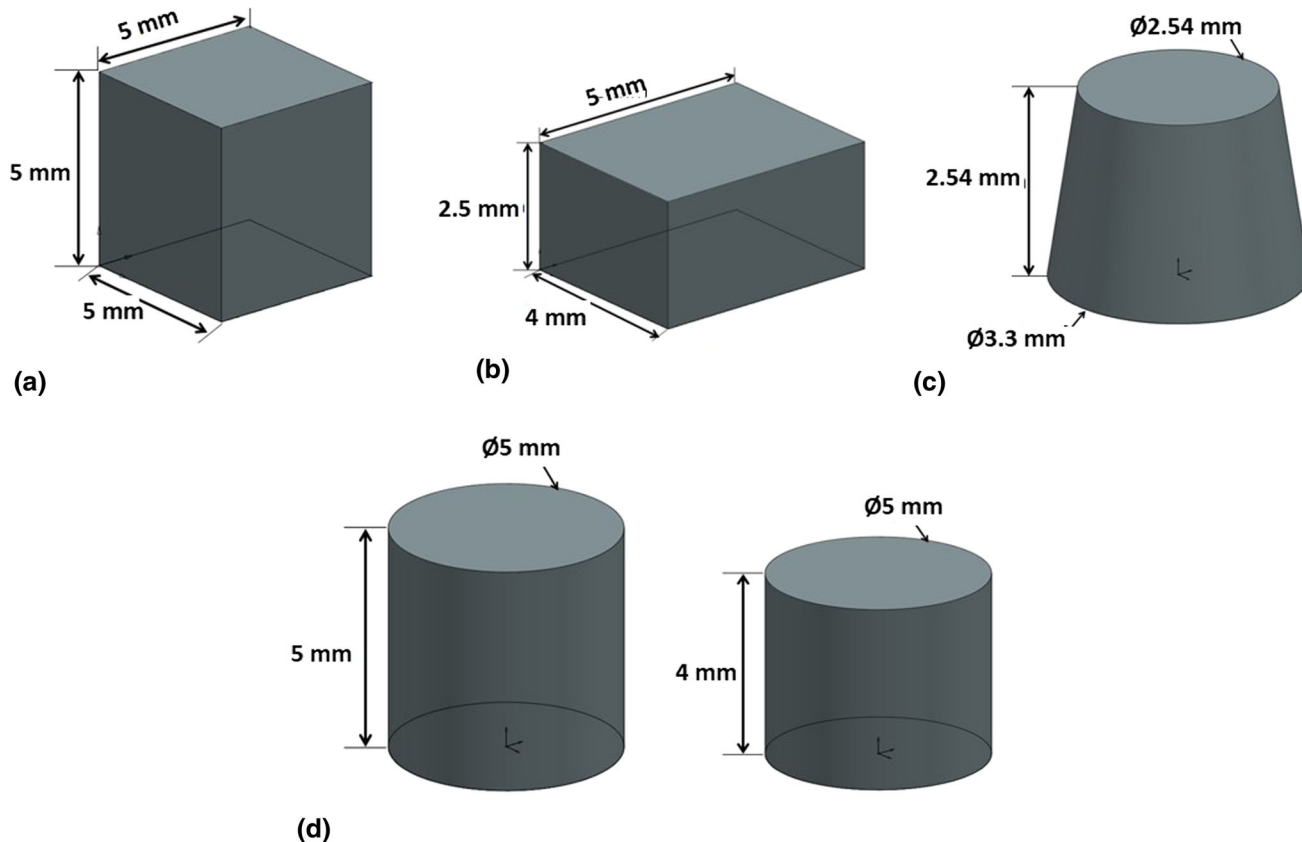
these directions. Since AA 2219 is an aluminum containing high content of copper ( $> 6\%$ ), the fine precipitates contributing to the high strength of the alloy in the peak-aged condition are predominantly  $\theta$  and  $\theta'$  phases, while the second phase particles will also be predominantly  $\text{Cu}_2\text{Al}$  (Ref 4, 5). The rather coarse second phase particles contribute little to the strengthening of the alloy and can be detrimental to strength if they form a network (Ref 6). The second phase particles can also form galvanic couple with the  $\alpha$ -aluminum phase and cause galvanic corrosion of the alloy in the presence of an electrolyte (Ref 7, 8).

Adiabatic shear bands (ASBs) develop in a material undergoing high strain-rate deformation when heat generated in some regions is not conducted away leading to thermomechanical instability and intense strain localization. Failure of metallic alloys at high strain rates is triggered by development of ASBs, along which cracks are initiated and rapidly propagated to cause catastrophic failure (Ref 9, 10). Cracks are initiated by microvoids generated inside the ASBs as a result of tensile stresses exerted on the shear bands during the impact loading. The tensile stresses are developed as a result of the difference in the strength of the viscoplastic shear band region and the surrounding rigid material (Ref 11, 12). The results of a metallographic analysis traced the failure of a propellant tank made of AA 2219 aluminum alloy to formation and cracking of ASBs (Ref 13). Evidence of local melting in some regions of the fracture surface provided an indication of the intensity of localized heating and temperature rise in the shear band region. Investigation of transformed bands that formed in a similar aluminum-copper alloy (AA 2519-T8) using the transmission electron microscope by Gao et al. (Ref 14) indicated the bands to consist of fine equiaxed grains with

G.M. Owolabi, D.T. Bolling, H.A. Whitworth, and N. Yilmaz, Department of Mechanical Engineering, Howard University, Washington, DC. A.G. Odeshi, Mechanical Engineering, University of Saskatchewan, Saskatoon, Canada; and A.G. Odeshi, Department of Civil Engineering, University of District of Columbia, Washington, DC. Contact e-mail: gbadabo.owolabi@howard.edu.

**Table 1** Nominal composition of AA 2219 aluminum alloy

Component	Al	Cu	Fe	Mg	Mn	Si	Ti	V	Zn	Zr
Wt.%	91.5-93.8	5.8-6.8	≤ 0.3	≤ 0.02	0.2-0.4	≤ 0.2	0.02-0.1	0.05-0.15	≤ 0.1	0.1-0.25

**Fig. 1** Geometries of the test specimens. (a) Cubic, (b) cuboidal, (c) conical (frustum), (d) cylindrical

average diameter of about 2  $\mu\text{m}$ . Depending on alloy composition and strain rates, both deformed shear bands consisting of severely deformed grains and transformed shear bands consisting of fine equiaxed grains have been reported to develop in aluminum alloys (Ref 15-17). The fine equiaxed grains inside transformed bands in aluminum alloys are formed by dynamic recrystallization (DRX) (Ref 15, 17).

Besides the observations of ASBs in the microstructure of an exploded propeller tank made of AA 2219-T8 alloy by Jha et al. (Ref 13), not much work has been done on dynamic impact response of AA 2219 aluminum. This is an attractive material for defense application due to its high tensile strength over a wide range of temperature. It is therefore important to understand the dynamic impact response of this alloy if it is exposed to ballistic impact in military applications. In the current study, the deformation and failure of AA 2219 aluminum alloy at high strain rates in relation to adiabatic shear banding were investigated using split Hopkinson bar system, digital imaging correlation (DIC) technique and microscopy. The DIC enables strain measurement in situ as the deformation proceeded using high-speed cameras. The effects of specimen geometry on the development, geometry and cracking tendency of ASBs in the alloy were investigated, and the results are discussed in this paper.

## 2. Materials and Methods

The investigated AA 2219 aluminum alloy was tested in the as-received T8 temper condition. It is an aluminum-copper containing minor alloy additions of manganese, vanadium and zirconium. Transmission electron microscopic investigation of age-hardened AA 2219 alloy by Elgallad et al. (Ref 4) indicated that the alloy, when specimens subjected to two-step aging, contains both  $\theta$  and  $\theta'$  precipitates leading to high strength. On the other hand, it was reported to contain predominantly  $\theta'$  precipitates when subjected to one-step aging. The investigated AA 2219 aluminum alloy is a commercial alloy with nominal composition presented in Table 1. The alloy was machined into cylindrical, cubical and conical shaped test specimens with dimensions as presented in Fig. 1.

Instrumented split Hopkinson pressure bar (Fig. 2) was used in conducting the dynamic impact test. It consists of incident bar, transmitter bar, striker bar, a light gun and data acquisition system (strain conditioner/amplifier and digital oscilloscope). The incident and transmitter bars are made of Ti-6Al-4V alloy and are 12.7 mm in diameter and 1892 mm long. The specimens were sandwiched between the incident and transmitter bars. A striker bar fired by a light gun strikes the end of the incident bar not in contact with the specimen. The impact

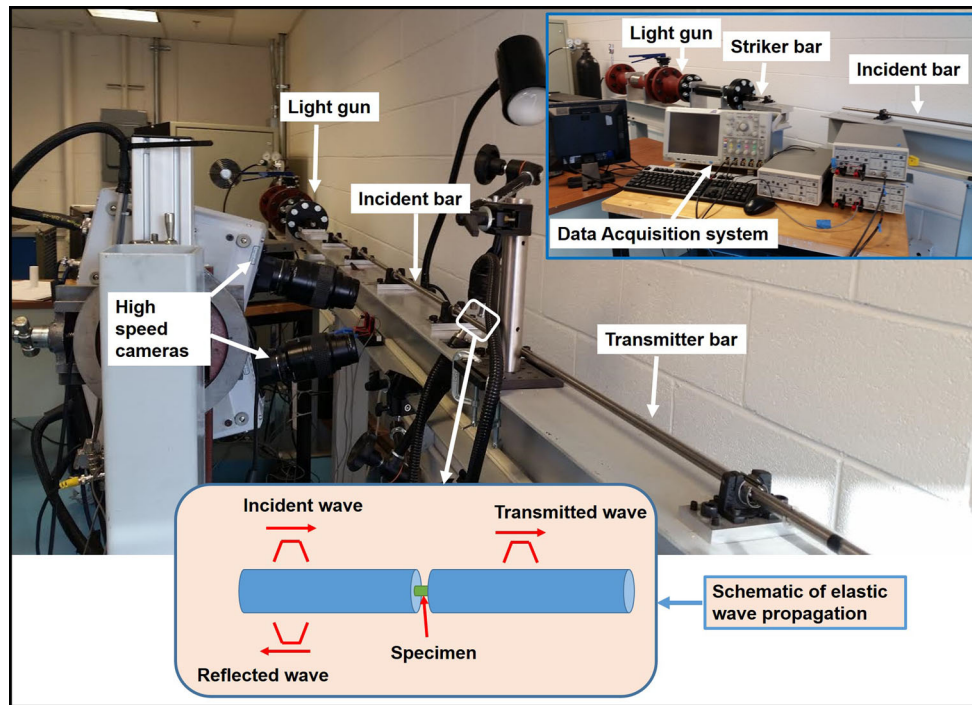


**Fig. 2** Experimental setup: split Hopkinson pressure bar synchronized with high-speed cameras for in situ strain measurement using digital image correlation technique

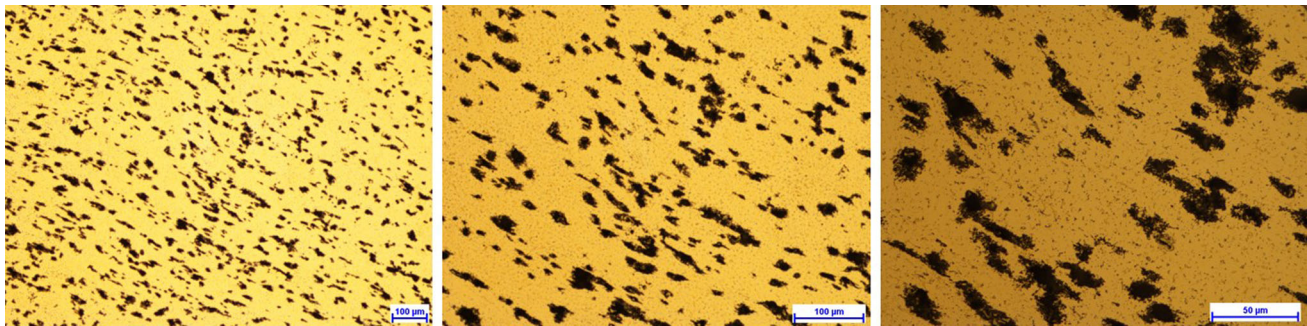


**Fig. 3** Optical micrographs of the as-received AA 2219-T8 aluminum alloy before impact

force generates elastic waves which travel through the incident bar. This is captured by a strain gage attached to the incident bar as incident wave. On reaching the test specimen, a fraction of the elastic wave is expended in rapidly deforming the specimen while a fraction is transmitted through the specimen on to the transmitter bar. The transmitted wave propagating through the transmitter bar is captured as transmitted wave by the strain gage attached to the transmitter bar. A fraction of the elastic wave is reflected at the contact between the specimens and the incident bar. These reflected waves are captured by the strain gage attached to the incident bar as reflected waves. A schematic representation of the wave propagation toward and away from the specimen is inserted in Fig. 2. The elastic strain data captured by the strain gages are processed by strain conditioner/amplifier connected to the strain and are stored by the connected mixed signal digital oscilloscope. The elastic strain data are used in the calculation of the strain ( $\epsilon$ ), stress ( $\sigma$ )

strain rates ( $\dot{\epsilon}$ ) in the specimens using the following equations (Ref 18):

$$\sigma = \left(\frac{A_B}{A_S}\right) E_B \epsilon_T \quad (\text{Eq 1})$$

$$\epsilon = -2 \left(\frac{C_B}{L_S}\right) \int_0^t \epsilon_R dt \quad (\text{Eq 2})$$

$$\dot{\epsilon} = -2 \left(\frac{C_B}{L_S}\right) \dot{\epsilon}_R \quad (\text{Eq 3})$$

where ( $\epsilon_I$ ),  $\epsilon_T$  and ( $\epsilon_R$ ) are incident, transmitted and reflected strain pulses, respectively,  $A_B$ ,  $C_B$  and  $E_B$  are cross-sectional area of the bars, wave propagation speed in the bars and elastic modulus of the bar material, respectively;  $A_S$  is the cross-sectional area of the specimens. For the conical specimens,  $A_S$  is taken to be the average of the cross section of the top

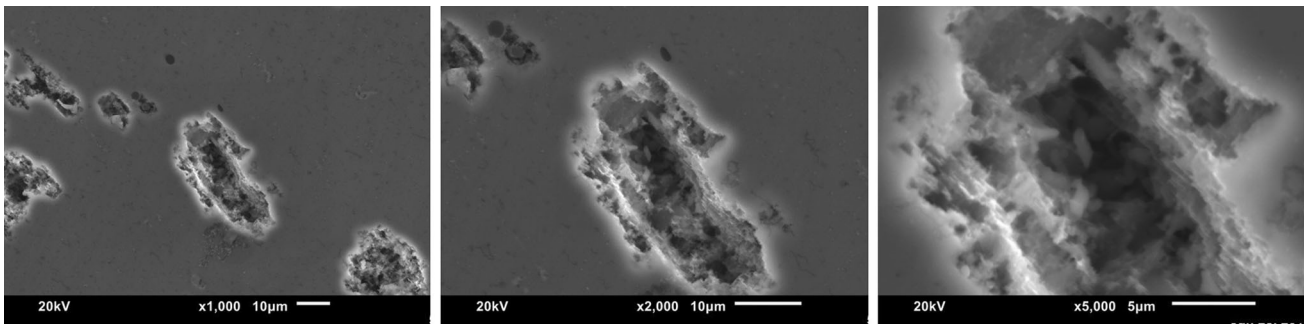


**Fig. 4** SEM micrographs of the as-received AA 2219-T8 aluminum alloy showing a second phase particle at different magnifications

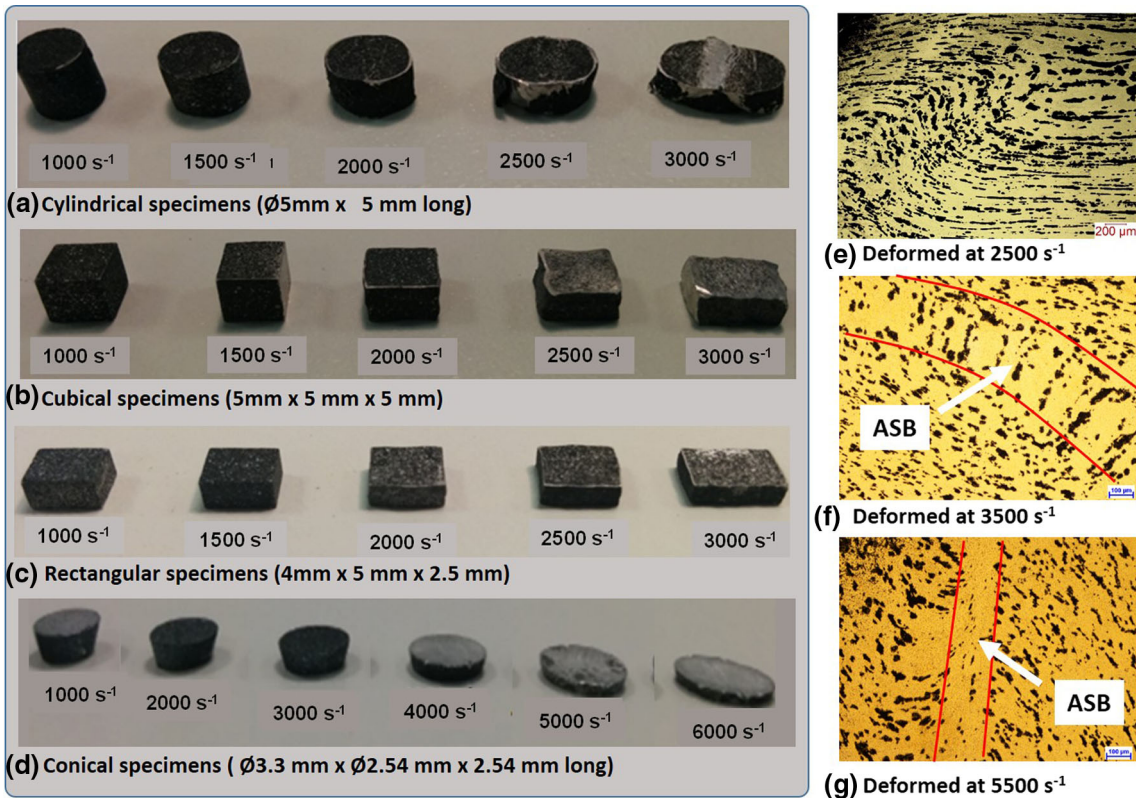


**Fig. 5** (a-d) Impacted specimens after plastic deformation at increasing strain rates and (e-g) microstructures showing the morphology of adiabatic shear bands in impacted Ø5 mm by 5 mm cylindrical specimens deformed at increasing strain rates

and base surfaces of conical the frustum, i.e.,  $A_s = \frac{\pi(R^2+r^2)}{2}$ . R and r are the radii of the base and top surfaces of the conical frustum, respectively.

In addition to the impact data provided by the data acquisition system connected to the SHPB, the digital image correlation (DIC) technique was used to capture strain in situ as the specimens deformed under the impact load. This was achieved through the use of two ultrahigh-speed Photron FastCam SA5 cameras (Fig. 2) that captured the images of the specimens during the high strain-rate deformation. To enable strain data to be effectively captured by the DIC during impact loading, the test specimens were coated with monochrome random dot pattern, which was achieved by painting with black and white patterns. The tracking of the displacement on the dot patterns was performed using ARAMIS (a commercial software developed by Trilion Quality System Inc.), which yields

accurate strain data. Metallurgical preparations of the alloy for microstructural examination involved cutting, grinding and polishing to mirror surface finish. This was followed by etching using a solution consisting of 25 ml ethanol, 25 ml HNO<sub>3</sub>, 25 ml HCl and 1 drop of HF.

### 3. Results and Discussion

#### 3.1 Microstructure of the As-Received Alloy

Optical micrographs indicating the microstructures of the as-received AA 2219-T8 aluminum alloy to consist of dispersed second phase particles in a continuous  $\alpha$ -aluminum phase are presented in Fig. 3. The second phase particles are formed as the solubility of the alloying elements in aluminum is exceeded

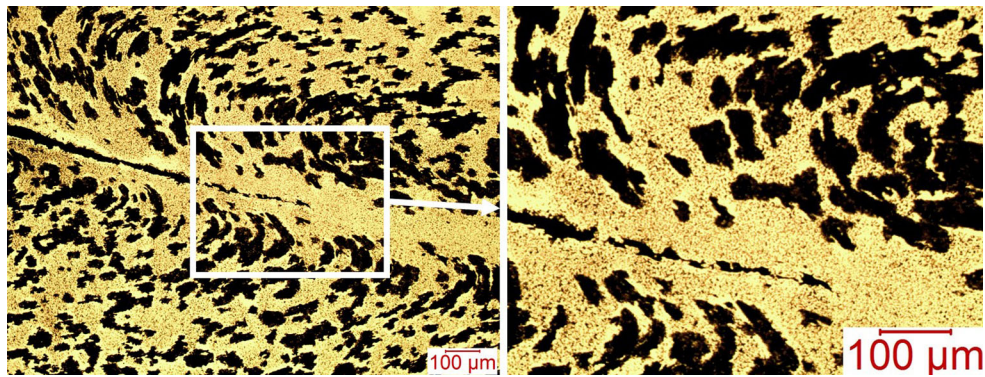


**Fig. 6** Crack propagation along a transformed shear band in an impacted AA 2219-T8 specimen

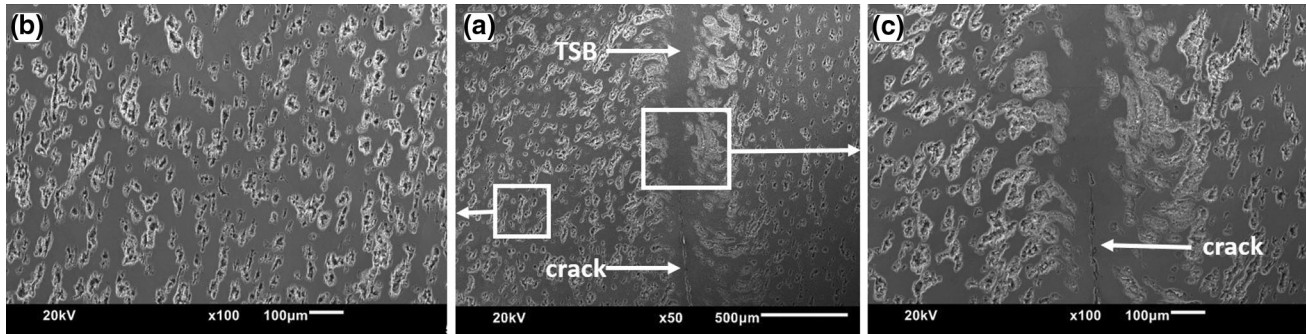


**Fig. 7** SEM micrograph of an impacted AA 2219 showing disappearance of second phase particles inside a transformed shear band (TSB): (a) overview, (b) outside TSB, (c) inside TSB

during cooling from the solidification temperature. Although the etchant could not reveal the grain boundaries, the morphology and distribution of the second phase particles are clearly revealed in the optical micrographs. There is a good contrast between the second phase particles and the continuous  $\alpha$ -aluminum phase. The second phase particles are widely dispersed within the  $\alpha$ -aluminum phase. They are mostly irregular in shape. Clustering of second phase particles was also observed in the microstructure (Fig. 3). The sizes of the second phase particles vary between 10 and 45  $\mu\text{m}$ , while the average particle size was calculated to be 22  $\mu\text{m}$ . The volume fraction of the second phase particles in the as-received alloy is estimated to be 6.8%. The scanning electron microscopic (SEM) micrographs (Fig. 4) suggest dissolution of the second phase particles by the etchant leaving behind groves in the areas containing second phase particles. It is important to note that x-ray diffraction or energy-dispersive spectroscopic analysis was not done to ascertain the composition of the second phase particles. A number of researchers, however, have used these techniques to identify  $\text{Al}_2\text{Cu}$  and  $\text{Al}_7\text{Cu}_2\text{Fe}$  (Ref 4, 5, 19) in aluminum-copper alloys containing such a large concentration of copper and negligible magnesium content as in the case of the investigated AA 2219 alloy. Manganese has the highest concentration of the minor alloying elements. Manganese in aluminum-copper alloy reacts with aluminum and copper to form  $\text{Al}_{20}\text{Cu}_2\text{Mn}_3$  dispersoids, which prevent grain growth during artificial aging heat treatment (Ref 6). Surekha et al. (Ref 8) identified the second phase particles in AA 2219 to be predominantly  $\text{Al}_2\text{Cu}$  intermetallic compound and reported that galvanic action between this compound and the continuous aluminum phase reduces the corrosion resistance of the alloy.

### 3.2 Microstructure of the Alloy After Dynamic Impact Loading

The geometries and microstructures of the test specimens after plastic deformation at increasing strain rates under impact loading are presented in Fig. 5. The geometry of the transverse section normal to the impact direction changed as the strain rate was increased. The circular shape of the transverse cross section of the cylindrical specimens and conical specimens changed to elliptical shape (Fig. 5a and d), while the square shape of the impacted plane of the cubical specimen became rectangular (Fig. 5b). The rectangular specimen became elongated in the direction of the longer side during impact loading. The severity of shape change increased with increase in strain rate. The change in shape is an indication of heterogeneous deformation in the specimens during impact loading. The deformation is relatively homogeneous for all the specimens deformed at 1000  $\text{s}^{-1}$  as evident in the negligible shape change in specimens impacted at this strain rate. The intensity of the deformation heterogeneity increased with strain rates leading to the formation of ASBs, which are regions of intense shear strain localization in the alloy at higher strain rates (Fig. 5e-g). ASBs occur in the regions of intense adiabatic heating and thermal softening during the impact loading of the specimens.

The microstructure of the alloy changed from one consisting of homogenous distribution of second phase particles to one containing shear bands which contain little or no second phase particles (Fig. 5e-g). The amount of second phase particles inside the shear bands decreased as strain rates and intensity of strain localization increased. Deformed bands were first observed in all the specimens when the strain rate was raised

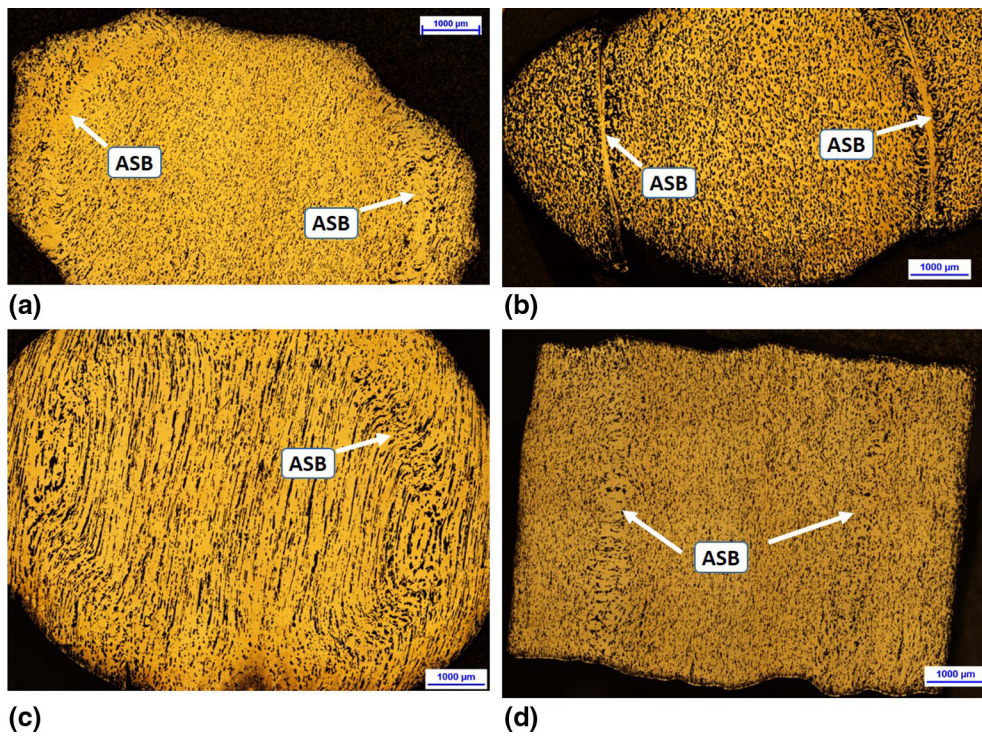


**Fig. 8** Optical micrographs showing the shapes of shear bands on the compression planes of the impacted specimens. Strain rates are provided in the bracket. (a) Ø5 mm × 4 mm cylindrical specimen ( $6000 \text{ s}^{-1}$ ), (b) Ø5 mm × 5 mm cylindrical specimen ( $3500 \text{ s}^{-1}$ ), (c) 3.5 mm × 2.5 mm conical specimen ( $6000 \text{ s}^{-1}$ ), (d) 5 mm × 5 mm × 5 mm conical specimen ( $3000 \text{ s}^{-1}$ )

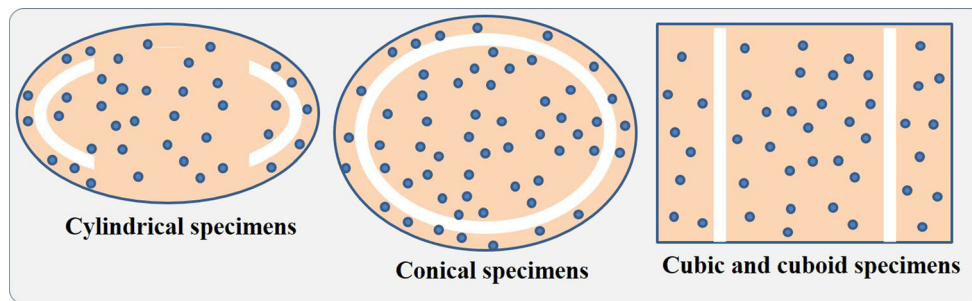


**Fig. 9** Schematic representation of the geometries of the fully developed transformed bands as a function of the shape of the impacted specimens

to  $2500 \text{ s}^{-1}$ . The critical strain rates at which transformed bands formed were observed to be dependent on the specimen geometry. Fully developed transformed bands were observed when the strain rates were increased to  $3000 \text{ s}^{-1}$  in the Ø5 mm × 5 mm cylindrical specimens, whereas a fully developed transformed band was not observed in the Ø5 mm × 4 mm until the strain rate was increased to  $5500 \text{ s}^{-1}$ . Only deformed bands were observed in the conical specimens impacted at  $6000 \text{ s}^{-1}$ . The micrographs in Fig. 5 provide indication of how the shear bands evolved as the strain rate was raised from 1000 to  $6000 \text{ s}^{-1}$  in Ø5 mm × 5 mm long cylindrical specimens. Strain localization began with alignment of second phase particles in shear flow direction forming an S-shape (Fig. 5e). As the intensity of shear strain and strain localization increased, the density of second phase particles in the shear bands decreased and remaining particles became aligned perpendicular to the shear band propagation path (Fig. 5f). Eventually fully developed transformed bands are

formed with minimal amount of second phase particles (Fig. 5g), suggesting dissolution of these particles inside the transformed bands. It has been suggested that deformed bands change to transformed bands as the intensity of strain localization, and consequently strain values, in the shear band reached a critical value (Ref 20). Thus, it can be concluded that the transformed bands observed at high strain rates developed from the deformed bands that initially formed at the onset of strain localization.

Both optical micrographs (Fig. 6) and SEM micrographs (Fig. 7) confirm dissolution of the second phase particles inside fully developed transformed bands. This suggests that the temperature reached inside the shear band is higher than the solvus temperature for the alloy, which is above  $500 \text{ }^\circ\text{C}$  under atmospheric pressure. Dissolution of second phase particles has been reported to be associated with the formation of transformed shear bands in other aluminum alloys during dynamic shock loading (Ref 10, 17). Crack initiation and propagation

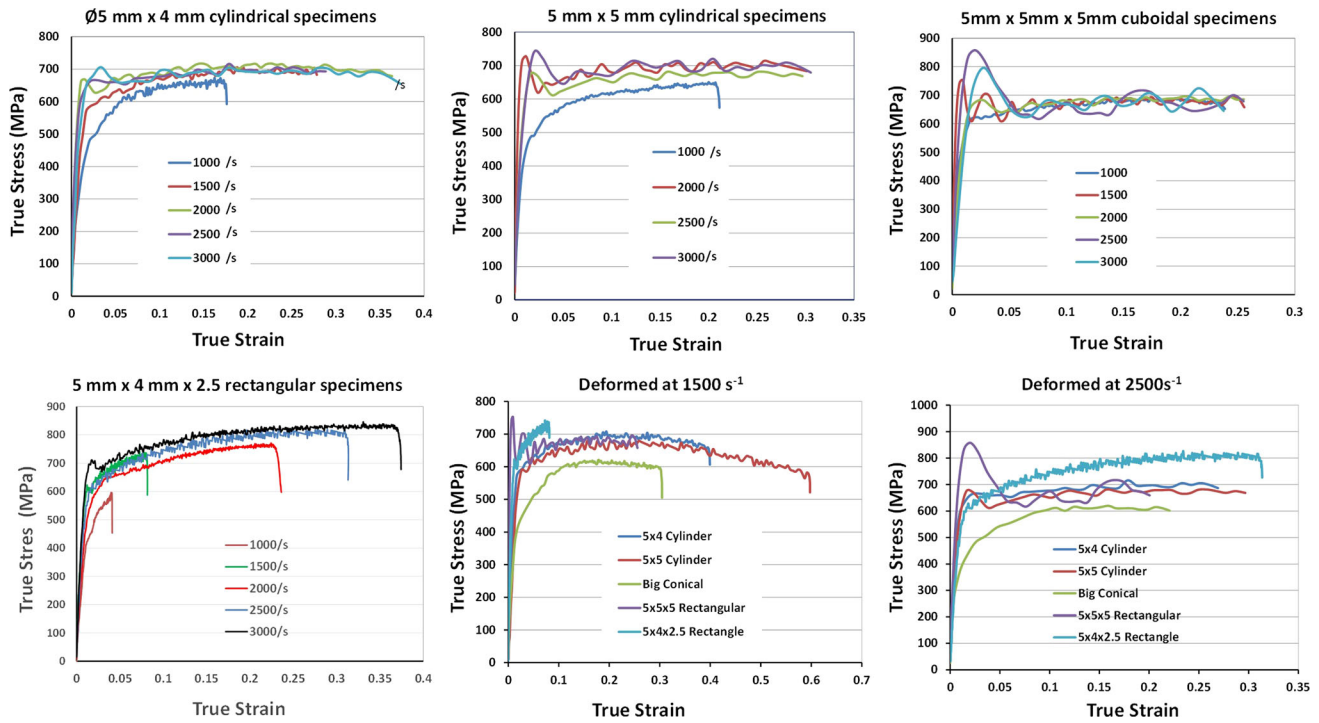


Fig. 10 Dynamic impact stress–strain curves for the AA 2219-T8 alloy

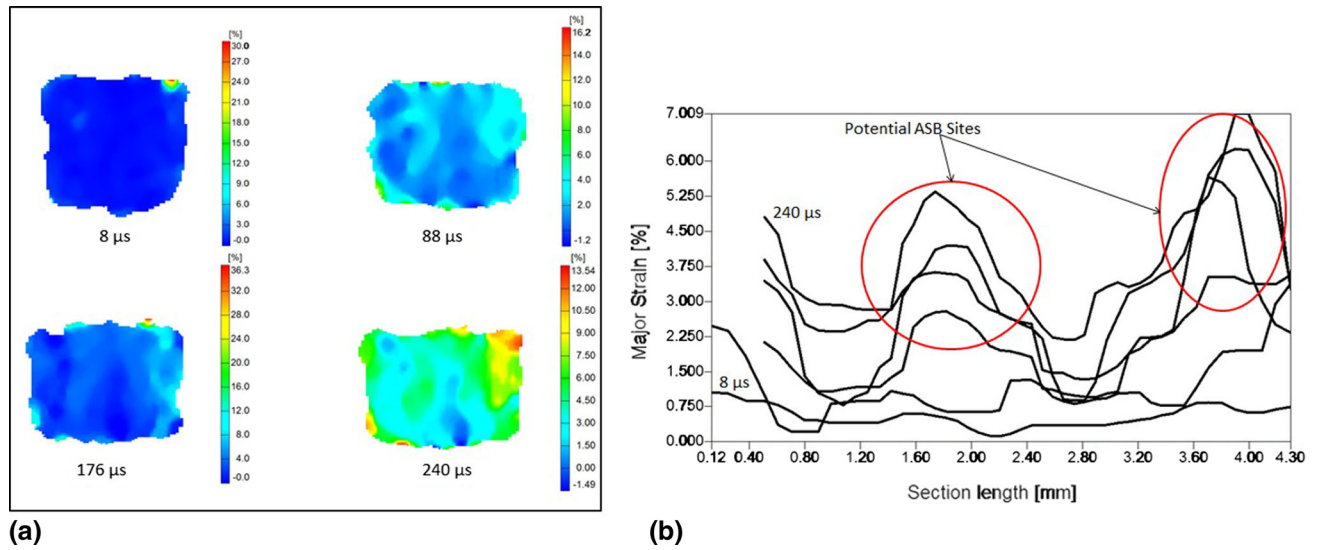
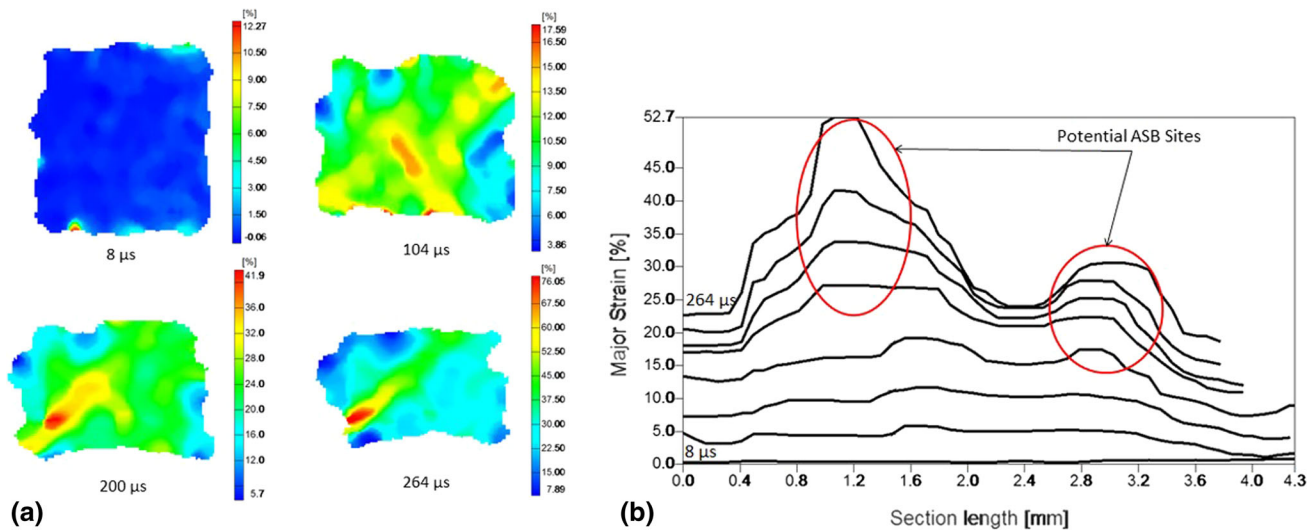


Fig. 11 (a) Strain distribution, (b) progression of strain distribution for Ø5 mm × 4 mm cylindrical specimen impacted at 1000 s<sup>-1</sup>

leading to fragmentation of the specimens occurred along the transformed bands (Fig. 6). Microvoids interconnected by microcracks were observed at the crack tip suggesting that the mechanism of crack formation inside the transformed bands involves microvoid nucleation and growth leading to formation of cracks connecting the microvoids. Similar crack initiation and propagation mechanism was reported in transformed bands of impacted AISI 4340 steel (Ref 21). The intense strain and adiabatic heating that occur in the shear bands during impact loading may be responsible for the dissolution of the coarse second phase particles. An analysis by Chen et al. (Ref 22) shows that temperature increase in excess of 1500 °C occurred in the transformed bands in Weldox 460E steel. Melting was

reported to occur inside the transformed shear bands that developed in AISI 4340 and 1340 steels under dynamic impact loading (Ref 23). These observations underscore the intensity of adiabatic heating that lead to formation of transformed shear bands in metallic alloys. Xu et al. (Ref 17) also suggested that dissolution of the second phase particles in AA 8090 aluminum alloy in transformed bands is an indication of the temperature inside the transformed bands exceeding the solvus temperature.

Optical micrographs showing geometries of the adiabatic shear bands on the compression plane of the impacted specimens are provided in Fig. 8, while schematic representation of the geometries of shear bands as a function of the shape of the test specimens is provided in Fig. 9. The white thick



**Fig. 12** (a) Strain distribution, (b) progression of strain distribution for 5 mm × 5 mm × 5 mm cubic specimen impacted at 1000 s<sup>-1</sup>

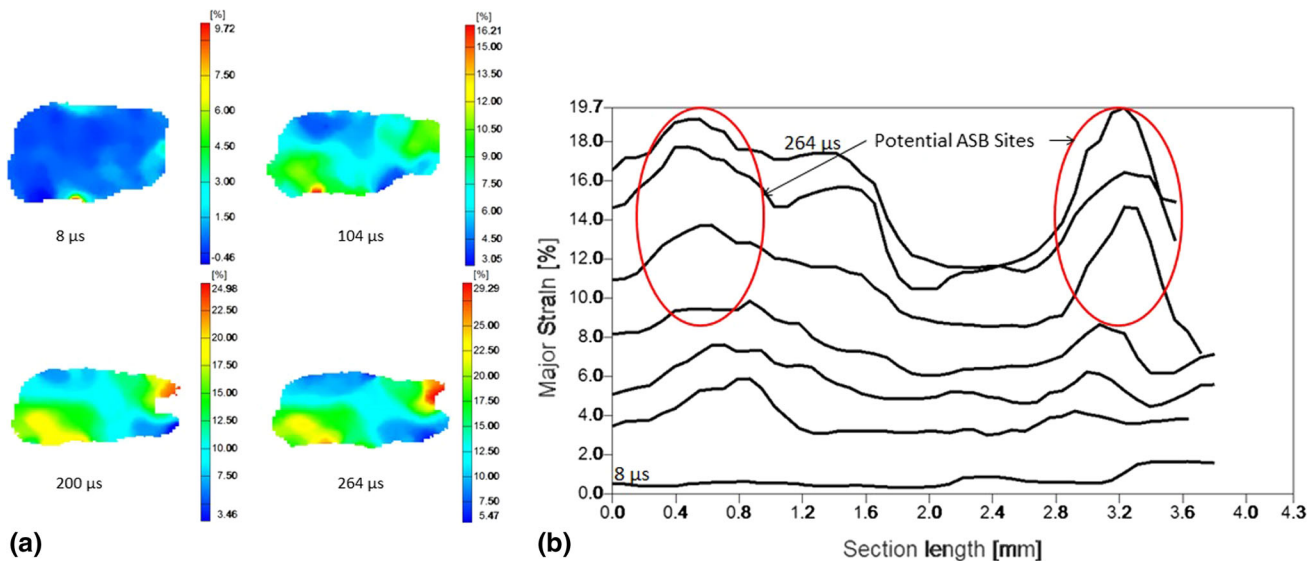


**Fig. 13** (a) Strain distribution, (b) progression of strain distribution for 5 mm × 5 mm × 4 mm rectangular specimen impacted at 2000 s<sup>-1</sup>

lines in Fig. 9 represent the fully transformed bands, while the dark particles represent the second phase particles. As observed in the micrographs, fully developed transformed bands are devoid of second phase particles in the schematic representation of the bands. The geometry of the adiabatic shear bands depends on the initial geometry of the specimens. The shear bands formed two elliptical vertices facing each other on the compression planes of the cylindrical specimens, whereas the shape of the shear bands on the compression planes of the conical specimens is elliptical (elongated circle). Two parallel shear bands were observed on the compression plane of cubical specimens. In AISI 1340 steel, the shape of the shear bands on the compression plane of a cuboidal test specimen was rectangular, whereas it was circular in cylindrical specimens of this steel (Ref 23). This implies that the geometry of adiabatic shear bands in impacted specimens is not only dependent on the geometry of the test specimens, but also on the type of alloy. The occurrence of the shear bands is

responsible for the change in the geometry of the compression plane of the impacted specimens. The cylindrical specimens that showed the greatest propensity to form transformed bands exhibited the greatest shape change.

### 3.3 Dynamic Stress–Strain Curves and DIC Measurements

The stress–strain curves obtained from the dynamic impact tests of the specimens as a function of strain rates and specimen geometry are provided in Fig. 10. The flow stress increased marginally as the strain rate was increased from 1000 to 3000 s<sup>-1</sup>. The average flow stress was determined to be approximately 700 MPa for most of the specimens. The rectangular specimens, however, attained a maximum flow stress of about 800 MPa at strain rates of 2500 and 3000 s<sup>-1</sup>. The total strain in the specimens increased significantly as the strain rate was increased. For example, the total strain of the rectangular specimen increased by 460% when the strain rate was doubled from 1500 to 3000 s<sup>-1</sup>. The marginal increase in



maximum flow stress as the strain rate was increased is attributed to the domineering influence of thermal softening over strain hardening during plastic deformation of the alloy at high strain rates. The higher the impact load, and consequently the strain rate, the higher will be the degree of thermal softening which cancels the strain hardening effect of plastic deformation. The increase in temperature leading to thermal softening is due to the conversion of most of the impact energy to heat energy in the specimens. Analysis has indicated that 90% of the kinetic energy of a projectile is converted to thermal energy when it strikes a target (Ref 24). The rest are either utilized in deforming the target or stored as residual strain energy in the target. It is evident from the stress-strain curves that plasticity of the alloy is significantly enhanced by thermal softening at high strain rates. The relatively good impact strength (700–800 MPa) of the investigated AA 2219 alloy can be traced to its T8 temper condition in which both strengthening effects of cold work and precipitation hardening are combined. The major strengthening precipitates in Al-Cu alloy, such as the investigated AA2219 alloy, are  $\theta$  and  $\theta'$  (Ref 4, 5). These precipitates are, respectively, coherent and semi-coherent with the continuous  $\alpha$ -aluminum phase. They are therefore very effective in hindering the dislocation motion and thereby increase the resistance to plastic deformation.

The results of the digital imaging correlation (DIC) measurement showing strain distribution maps and strain values across the length of some test specimens during deformation under impact loading are presented in Figs. 11, 12, and 13. The strain distribution images and plots were obtained by post-processing of the strain data captured by the DIC system using ARAMIS, the DIC commercial software from Trilion Quality System Inc. The graph was created by taking a horizontal line section in the middle of the shear localization stages calculated by ARAMIS software. The section established a series of data collection points along the specimen's horizontal length relative to the visual images that were previously processed. Each individual curve on the resulting graph represents the strain data along the section line at different times during the compression. The plot is another useful way of monitoring heterogeneity of deformation along the test length of specimens in situ during impact, especially shear localization. Deformation which was uniform across the length of the specimens started showing evidence of strain localization as strain values in some region became higher than the adjacent region. The time at which the strain localization became pronounced, the location and the intensity of localization varied slightly with specimen geometry and strain rate. Potential sites for shear strain localization leading to formation of adiabatic shear bands (marked with read circles in the figures) can be recognized along the length of the specimens from the strain distribution maps and plots.

#### 4. Conclusion

Cylindrical, cuboidal and conical specimens of AA 2219 aluminum alloy were subjected to dynamic impact test using the split Hopkinson pressure bar synchronized with digital image correlation system. Heterogenous deformation of the alloy occurred at high strain rates resulting in intense strain localization and formation of adiabatic shear bands. Deformed bands were first observed in the test specimens when

the strain rate was raised to  $2500 \text{ s}^{-1}$ . Initially the deformed bands consisted of second phase particles aligning in shear flow direction forming what looked like S-shape. As the intensity of adiabatic heating and strain localization increased at higher strain rates, the particles aligned perpendicular to the shear band propagation path. The concentration of the second phase particles in the shear bands decreased as the strain rate increased. Eventually transformed bands devoid of second phase particles developed at high strain rates, suggesting particle dissolution inside the transformed bands. The critical strain rates for formation of transformed bands and their shape on the compression planes varied depending on the geometry of the test specimens. Failure of the specimens occurred by ductile fracture characterized by formation of microvoids inside the transformed bands, which became connected to form crack propagating along the transformed bands.

#### Acknowledgments

The authors would like to acknowledge the financial support from the Department of Defense through the research and educational program HBCU/MSI (Contract #W911NF-15-1-0457) under the direct supervision of Patricia A. Huff (Program Manager, ARO HBCU/MI Program Manager).

#### References

1. G.V. Narayana, V.M.J. Sharma, V. Diwakar, K.S. Kumar, and R.C. Prasad, Fracture Behaviour of Aluminium Alloy 2219-T87 Welded Plates, *Sci. Technol. Weld. Join.*, 2004, **9**(2), p 121–130
2. C.V.A. Narasayya, P. Rambabu, M.K. Mohan, R. Mitra, and N.E. Prasad, Tensile Deformation and Fracture Behaviour of an Aerospace Aluminium Alloy AA2219 in Different Ageing Conditions, *Procedia Mater. Sci.*, 2014, **6**, p 322–330
3. A.K. Jha, P.R. Narayanan, and K. Sreekumar, Liquefaction Cracking of Al-6.3 Cu Alloy Propellant Storage Tank—A Case Study, *Eng. Fail. Anal.*, 2009, **16**(5), p 1587–1596
4. E.M. Elgallad, Z. Zhang, and X.-G. Chen, Effect of Two-Step Aging on the Mechanical Properties of AA2219 DC Cast Alloy, *Mater. Sci. Eng. A*, 2015, **625**, p 213–220
5. V.M.J. Sharma, K.S. Kumar, B.N. Rao, and S.D. Pathak, Effect of Microstructure and Strength on the Fracture Behavior of AA2219 Alloy, *Mater. Sci. Eng. A*, 2009, **502**(1-2), p 45–53
6. M. Warmuzek, Metallographic Techniques for Aluminum Alloys, in *ASM Handbook: Metallography and Microstructure*, vol. 9, ASM International, Materials Park, OH, 2004, p 711–751
7. K. Surekha, B.S. Murty, and K.P. Rao, Comparison of Corrosion Behaviour of Friction Stir Processed and Laser Melted AA 2219 Aluminium Alloy, *Mater. Des.*, 2011, **32**(8-9), p 4502–4508
8. K. Surekha, B.S. Murty, and K.P. Rao, Effect of Processing Parameters on the Corrosion Behaviour of Friction Stir Processed AA 2219 Aluminum Alloy, *Solid State Sci.*, 2009, **11**(4), p 907–917
9. G. Owolabi, D. Odoh, A. Odeshi, and H. Whitworth, Occurrence of Dynamic Shear Bands in AISI, 4340 Steel Under Impact Loads, *World J. Mech.*, 2013, **03**(02), p 139–145
10. A.G. Odeshi, A.O. Adesola, and A.Y. Badmos, Failure of AA 6061 and 2099 Aluminum Alloys Under Dynamic Shock Loading, *Eng. Fail. Anal.*, 2013, **35**, p 302–314
11. C.L. Wittman, M.A. Meyers, and H.-R. Pak, Observation of an Adiabatic Shear Band in AISI 4340 Steel by High-Voltage Transmission Electron Microscopy, *Metall. Trans. A*, 1990, **21**, p 707–716
12. M.A. Meyers, Dynamic Failure: Mechanical and Microstructural Aspects, *J. Phys. III*, 1994, **C8**, p 597–621
13. A.K. Jha, S.V.S.N. Murty, K. Sreekumar, and P.P. Sinha, High Strain Rate Deformation and Cracking of AA 2219 Aluminium Alloy Welded Propellant Tank, *Eng. Fail. Anal.*, 2009, **16**(7), p 2209–2216

14. Z. Gao, X. Zhang, Y. Zhao, M. Chen, and H. Li, The Effect of Strain Rate on the Microstructure of 2519A Aluminium Alloy Plate Impacted at 573 K, *J. Alloys Compd.*, 2009, **481**, p 422–426
15. D. Zhu, Z. Zheng, and Q. Chen, Adiabatic Shear Failure of Aluminum Matrix Composites and Microstructural Characteristics of Transformed Bands, *Mater. Sci. Eng. A*, 2014, **595**, p 241–246
16. Y. Yang, H.G. Zheng, Z.J. Shi, and Q.M. Zhang, Effect of Orientation on Self-Organization of Shear Bands in 7075 Aluminum Alloy, *Mater. Sci. Eng., A*, 2011, **528**(6), p 2446–2453
17. Y.B. Xu, W.L. Zhong, Y.J. Chen, L.T. Shen, Q. Liu, Y.L. Bai, and M.A. Meyers, Shear Localization and Recrystallization in Dynamic Deformation of 8090 Al-Li Alloy, *Mater. Sci. Eng. A*, 2001, **299**(1-2), p 287–295
18. S. Nemat-Naser, Introduction to high strain rate tension and compression tests, in *ASM Handbook*, vol. 8 (2000), pp. 942–955
19. S. Roy, B.R. Nataraj, S. Suwas, S. Kumar, and K. Chattopadhyay, Microstructure and Texture Evolution During Accumulative Roll Bonding of Aluminium Alloys AA2219/AA5086 Composite Laminates, *J. Mater. Sci.*, 2012, **47**(17), p 6402–6419
20. A.O. Adesola, A.G. Odeshi, and U.D. Lanke, The Effects of Aging Treatment and Strain Rates on Damage Evolution in AA 6061 Aluminum Alloy in Compression, *Mater. Des.*, 2013, **45**, p 212–221
21. M.N. Bassim and A.G. Odeshi, Shear Strain Localisation and Fracture in High Strength Structural Materials, *Arch. Mater. Sci. Eng.*, 2008, **31**(2), p 69–74
22. X.W. Chen, Q.M. Li, and S.C. Fan, Initiation of Adiabatic Shear Failure in a Clamped Circular Plate Struck by a Blunt Projectile, *Int. J. Impact Eng.*, 2005, **31**(7), p 877–893
23. H.M. Ghomi and A.G. Odeshi, The Effects of Microstructure, Strain Rates and Geometry on Dynamic Impact Response of a Carbon-Manganese Steel, *Mater. Sci. Eng. A*, 2012, **532**, p 308–315
24. J.F.C. Lins, H.R.Z. Sandim, H.-J. Kestenbach, D. Raabe, and K.S. Vecchio, A Microstructural Investigation of Adiabatic Shear Bands in an Interstitial Free Steel, *Mater. Sci. Eng. A*, 2007, **457**(1-2), p 205–218